Channel Characterization for Wideband Large-Scale Antenna Systems Based on a Low-Complexity Maximum Likelihood Estimator

Ji, Yilin; Fan, Wei; Pedersen, Gert F.

Published in:
I E E E Transactions on Wireless Communications

DOI (link to publication from Publisher):
10.1109/TWC.2018.2854553

Publication date:
2018

Document Version
Accepted author manuscript, peer reviewed version

This article has been accepted for publication in a future issue of this journal, but has not been fully edited. Content may change prior to final publication. Citation information: DOI 10.1109/TWC.2018.2854553, IEEE Transactions on Wireless Communications

Channel Characterization for Wideband Large-Scale Antenna Systems Based on a Low-Complexity Maximum Likelihood Estimator

Yilin Ji, Wei Fan, Gert F. Pedersen

***Abstract*—Wideband large-scale array systems operating at millimeter-wave bands are expected to play a key role in future communication systems. It is recommended by standardization groups to use spherical-wave models (SWMs) to characterize the channel in near-field cases because of the large array apertures and the small cell size. However, this feature is not widely reflected in channel models yet, mainly due to the high computational complexity of SWMs compared to that of the conventional plane-wave model (PWM), especially when ultrawideband signals are considered. In this paper, a maximum likelihood estimator (MLE) of low computational complexity is implemented with a SWM for ultrawideband signals. The measurement data obtained from an ultrawideband large-scale antenna array system at 28-$30\,\mathrm{GHz}$ are processed with the proposed algorithm. The power azimuth-delay profiles (PADP) estimated from the SWM and the PWM are compared to those obtained from rotational horn antenna measurement, respectively. It shows that the multipath components (MPCs) are well-estimated with the proposed algorithm, and significant improvement in estimation performance is achieved with the SWM compared to the PWM. Moreover, the physical interpretation of the estimated MPCs is also given along with the estimated scatterers.**

***Index Terms*—Spherical-wave signal model, ultrawideband, millimeter wave, channel estimation.**

I. Introduction

FOR the upcoming fifth generation (5G) communication systems or future generations, it has been predicted that key features, including massive multiple-input multiple-output (MIMO) systems and high frequency bands (above $6\,\mathrm{GHz}$), will be crucial to increase the system capacity. With a large-scale antenna array system (e.g. array with tens to hundreds of elements) [1], the beamwidth of the beamforming technique can be ultra-narrow, which increases the spatial degrees of freedom of the system [2]. In addition, the high array gain is also beneficial to compensate the high propagation loss at high frequency bands. For multi-user scenarios, the system ability to serve a number of users over the same frequency and time resources through spatial multiplexing at the base station will be improved, and a higher spectral efficiency can be achieved. On the other hand, the rich spectrum resource at high frequency bands is also a key to deliver high capacity.

In order to exploit wideband large-scale antenna array systems, it is necessary to measure and characterize the underlying propagation channels. Channel measurement techniques can be generally separated into two categories, namely the time-domain sounding techniques [3]–[9], and the frequency-domain sounding techniques [6], [10], [11]. The time-domain sounding techniques have the advantage of fast measurement speed, which makes them suitable for measuring time-variant channels [12], [13]. However, time-domain channel sounders are usually designed for specific measurement requirements such as measurement frequency and bandwidth. Once the time-domain sounder is implemented, it typically would need much effort to modify it for different measurement requirements. On the contrary, the frequency-domain channel sounders, which are usually vector network analyzer (VNA) based, are more flexible in this regard. Measurement frequency and bandwidth can be set to any desired value supported by the VNA systems, which makes the VNA-based sounders versatile for different frequencies. Therefore, the VNA-based sounders are quite popular among research groups for ultrawideband measurement at high frequency bands [6], [14]–[16]. The relatively slow measurement speed for frequency sweeping is a drawback of the VNA-based sounder, which makes it inappropriate to measure time-variant channels.

There are some new challenges for channel estimation algorithms. Two assumptions usually adopted for channel estimation are probably violated for wideband large-scale antenna array systems, namely the far-field assumption and the narrowband assumption. The far-field assumption holds when the distance between the scattering source and the antenna array is larger than the so-called near-field outer boundary, which is also known as the Fraunhofer distance. In the literature [17]–[20], there are several definitions for the near-field outer boundary, among which $2D^2/\lambda$ is most frequently used, where D is the array aperture in meters, and λ is the wavelength in meters [17]. Under this definition, a uniform linear array of 100 elements with half-wavelength inter-element spacing operating at $30\,\mathrm{GHz}$ has a near-field outer boundary of nearly $50\,\mathrm{m}$, which covers the scope of many short-range application scenarios [21]. Basically, the significance of the spherical wavefront observed at the array increases as the scattering sources getting closer to the array. In order to reduce the model mismatch from the plane-wave model (PWM) for channel estimation, the spherical-wave model (SWM) can be used instead. In many standardization organizations and research groups, it is recommended to use SWMs to characterize channels for near-field cases [22]–[25]. Moreover, some measurement results also showed the necessity of utilizing SWM, e.g. see in [26]–[28].

The authors are with the APMS section at the Department of Electronic Systems, Falculty of Engineering and Science, Aalborg University, Denmark. Email: {yilin, wfa, gfp}@es.aau.dk. (Corresponding author: Wei Fan.)

This article has been accepted for publication in a future issue of this journal, but has not been fully edited. Content may change prior to final publication. Citation information: DOI 10.1109/TWC.2018.2854553, IEEE Transactions on Wireless Communications

The narrowband assumption holds when the condition $D/\lambda \ll f/B$ is satisfied, where f is the frequency and B is the bandwidth [29]. When the bandwidth becomes so wide (e.g. several GHz) that the narrowband assumption does not hold anymore for a given array aperture and frequency, the propagation delay of a single multipath component (MPC) can be resolved at different delay bins between array elements. Therefore, the array steering vector should be calculated with respect to each frequency point instead of the center frequency for channel estimation. In the literature [30], the term "ultrawideband" is usually defined as either the relative bandwidth is larger than $20\,\%$ or the absolute bandwidth is larger than $500\,\mathrm{MHz}$. However, it is not directly related to the array aperture by its definition. Therefore, in this paper, we use the term "wideband" to refer to the case where the narrowband assumption does not hold.

For the SWM, signals are assumed to be radiated from point sources. The phase difference between array elements is usually calculated based on the law of cosines according to the distance from the point sources to the array elements [26]. In the literature, the SWM has been applied to many source localization applications [18], [28], [31]–[34] with different estimation algorithms. Subspace based algorithms, such as the multiple signal classification algorithm (MUSIC) [35] and the estimation of signal parameters via rotational invariant techniques (ESPRIT) [36], have been adapted to estimate the locations of scatterers for narrowband scenarios in [18], [32], [37]. However, multi-dimensional estimation (e.g. joint delay-angle estimation) is hard to implement, since the computational complexity grows significantly as the size of the covariance matrix increases drastically with the number of estimation dimensions. Moreover, their estimation performance degrades severely when channel snapshots are not sufficient or coherent sources exist [29]. Maximum-likehood based algorithms, e.g. the space-alternating generalized expectation-maximization (SAGE) [38] and Richter's Maximum likelihood estimation (RiMAX) [39], have been proposed for the wideband signal with the SWM in [26], [28], [40]. Although these algorithms were not restricted by snapshot number or source correlation, the supported bandwidth is still bounded by the narrowband assumption. If the narrowband assumption does not hold due to large measurement bandwidth, the prerequisite for deploying the space-alternating mechanism would not be fulfilled [39], [41]. In [26], in order to enable the space-alternating mechanism, the wideband signal was divided into several subbands. In [28], the SAGE algorithm was implemented based on the SWM with the narrowband assumption fulfilled.

In our previous work [16], a measurement campaign was conducted with a virtual uniform circular array (UCA) with $2\,\mathrm{GHz}$ bandwidth at different frequencies. Using a virtual antenna array helps to reduce the mutual coupling effect between antenna elements for channel estimation [42]. The measurement data were processed with a classic (Bartlett) beamforming under the plane-wave assumption. It was shown that severe joint sidelobes exist in the power azimuth-delay profile (PADP) due to the frequency-variant array factor for huge bandwidths. To cope with the high joint sidelobes, a frequency-invariant beamformer was proposed for the UCA in [43]. However, the resulting PADP still suffers from high sidelobes for the detected dominant paths. In [27], a relaxed near-field outer boundary compared to $2D^2/\lambda$ was proposed, above which the PWM can still be used for estimating solely the angle information. In [44], a preliminary study on channel estimation based on the SWM was conducted. In order to eventually achieve a geometry-based stochastic channel model (GSCM) in connection to the 3rd generation partnership project (3GPP) [23], it is essential to obtain the multi-dimensional MPC parameters.

The main contributions of this paper are summarized as follows:

- A low-complexity maximum likelihood estimator (MLE) is proposed for wideband large-scale array systems. The proposed estimator works for the case where the far-field and the narrowband assumption are both violated.
- MPC parameters are estimated for indoor large-scale array measurements at 28-30 GHz.
- Comparison is made between the SWM and the PWM with the proposed MLE algorithm in terms of the estimation performance for the measurement data.
- Physical interpretation of the estimated MPCs is given along with the locations of the estimated scatterers in the environment.

The rest of the paper is organized as follows: Section II gives the generic signal model for wideband large-scale antenna array systems. Section III discusses the limitations of the widely deployed SAGE algorithm for wideband large-scale antenna array systems. Section IV describes the details of the proposed low-complexity MLE algorithm. Section V shows the estimation results for an indoor wideband large-scale array measurement, and Section VI concludes the paper.

The notation used in this paper is as follows: Scalars are shown in regular font, and vectors and matrices are in bold font. $(\cdot)^{\mathrm{T}}$ represents the transpose operator, $(\cdot)^{\mathrm{H}}$ the complex conjugate operator, $\|\cdot\|$ the Euclidean norm, $|\cdot|$ the absolute value operator, and $\mathrm{vec}\{\cdot\}$ denotes the vectorization operator which transforms a matrix into a column vector.

II. Signal Model for the Wideband SWM

When the SWM is considered, signals are assumed to be radiated from point sources [26]. Either a single antenna or a single scatterer can be regarded as a point source. Without loss of generality, here we assume that the transmitter (Tx) is equipped with a single antenna, and the receiver (Rx) is equipped with an M-element antenna array of an arbitrary structure (e.g. linear, circular, or rectangular). It follows that both the Tx antenna and the scatterers can be considered as the point sources in the environment, as illustrated in Fig. 1 along with the local coordinate system at the Rx side.

For a propagation channel consisting of L paths, the channel transfer function $\mathbf{H}(\boldsymbol{f};\boldsymbol{\Theta}_l) \in \mathbb{C}^{M\times K}$ of the l-th path over K frequency points $\boldsymbol{f} = [f_1, f_2, \ldots, f_K]$ can be expressed as [26]

$$\mathbf{H}(\boldsymbol{f};\boldsymbol{\Theta}_l) = \alpha_l \boldsymbol{s}(\boldsymbol{f};\phi_l,\theta_l,d_{0,l},\tau_l), \tag{1}$$

This article has been accepted for publication in a future issue of this journal, but has not been fully edited. Content may change prior to final publication. Citation information: DOI 10.1109/TWC.2018.2854553, IEEE Transactions on Wireless Communications

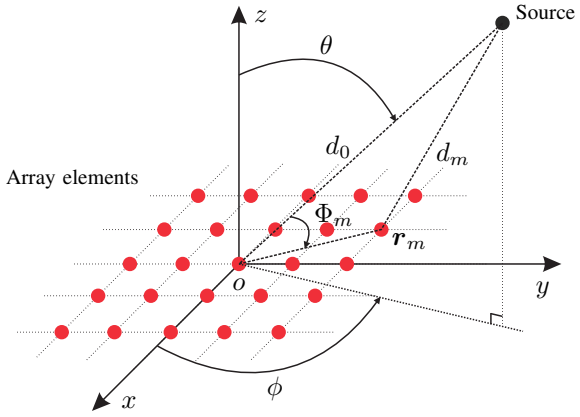

Fig. 1. Illustration of the SWM and the local coordinate system at the Rx side.

where $\boldsymbol{\Theta}_l = \{\alpha_l, \phi_l, \theta_l, d_{0,l}, \tau_l\}$ is the parameter set of the l-th path, including the complex amplitude α_l, the azimuth angle of direction of arrival ϕ_l, the elevation angle of direction of arrival θ_l, the distance $d_{0,l}$ from the source to the array center, and the delay τ_l from the Tx antenna to the Rx array center. The (m,k)-th component of $\boldsymbol{s}(\boldsymbol{f};\phi_l,\theta_l,d_{0,l},\tau_l) \in \mathbb{C}^{M\times K}$ can be written as

$$\begin{aligned} s_m(f_k;\phi_l,\theta_l,d_{0,l},\tau_l) =& \frac{g_m(f_k;\phi_l,\theta_l)}{4\pi f_k d_{m,l}/c} \\ &\cdot \exp\{-j2\pi f_k (d_{m,l}-d_{0,l})/c\} \\ &\cdot \exp\{-j2\pi f_k \tau_l\}, \end{aligned} \tag{2}$$

where $g_m(\cdot)$ is the antenna field pattern, c is the speed of light, and $d_{m,l}$ denotes the distance from the source to the m-th array element for the l-th path. Note when the source corresponds to the Tx instead of a scatterer, it leads to $\tau_l = d_{0,l}/c$. Given the coordinates $\boldsymbol{r}_m$ of the m-th array element with respect to the array center, the distance $d_{m,l}$ can be determined by applying the law of cosines as

$$d_{m,l} = \sqrt{d_{0,l}^2 + \|\boldsymbol{r}_m\|^2 - 2d_{0,l}\|\boldsymbol{r}_m\|\cos\Phi_{m,l}}\ , \tag{3}$$

where $\Phi_{m,l}$ denotes the angle between vector $\boldsymbol{r}_m$ and the direction of arrival of the l-th wave. For notation simplicity, we use $\boldsymbol{\Theta}_l^{\bar{\alpha}} = \{\phi_l, \theta_l, d_{0,l}, \tau_l\}$ to denote the parameter set without α_l, and $\boldsymbol{s}(\boldsymbol{f};\boldsymbol{\Theta}_l^{\bar{\alpha}})$ to represent $\boldsymbol{s}(\boldsymbol{f};\phi_l,\theta_l,d_{0,l},\tau_l)$ hereafter.

The measured channel frequency response $\mathbf{Y}(\boldsymbol{f}) \in \mathbb{C}^{M\times K}$ at the output of the Rx array can then be expressed as

$$\mathbf{Y}(\boldsymbol{f}) = \sum_{l=1}^{L} \mathbf{H}(\boldsymbol{f};\boldsymbol{\Theta}_l) + \boldsymbol{n}(\boldsymbol{f}), \tag{4}$$

where $\boldsymbol{n}(\boldsymbol{f}) \in \mathbb{C}^{M\times K}$ is the noise of the measurement system, and its entries are assumed to follow the independent and identically distributed (i.i.d.) complex white Gaussian distribution with zero mean and variance σ_n^2 [26]. To keep a compact notation, we further define

$$\mathbf{H}(\boldsymbol{f};\boldsymbol{\Theta}) = \sum_{l=1}^{L} \mathbf{H}(\boldsymbol{f};\boldsymbol{\Theta}_l), \tag{5}$$

with $\boldsymbol{\Theta} = \{\boldsymbol{\Theta}_1, \boldsymbol{\Theta}_2, \ldots, \boldsymbol{\Theta}_L\}$.

III. Limitations of the SAGE Algorithm for Wideband Large-scale Antenna Array Systems

For channels measured with conventional narrowband small-scale array systems, under the narrowband and the far-field assumptions, the channel transfer function $\mathbf{H}(\boldsymbol{f};\boldsymbol{\Theta}_l)$ in (1) can be simplified as [38]

$$\mathbf{H}(\boldsymbol{f};\tilde{\boldsymbol{\Theta}}_l) = \alpha_l \boldsymbol{v}(\phi_l,\theta_l) \otimes \boldsymbol{\zeta}(\boldsymbol{f};\tau_l) \tag{6}$$

where $\tilde{\boldsymbol{\Theta}}_l = \{\alpha_l, \phi_l, \theta_l, \tau_l\}$ denotes the parameter set with $d_{0,l}$ left out, and $\otimes$ denotes the Kronecker product. $\boldsymbol{v}(\phi_l,\theta_l) \in \mathbb{C}^{M\times 1}$ is the array steering vector with the m-th entry written as

$$v_m(\phi_l,\theta_l) = g_m(f_c;\phi_l,\theta_l)\exp\{j2\pi f_c \langle \boldsymbol{e}(\phi_l,\theta_l), \boldsymbol{r}_m\rangle\}, \tag{7}$$

where f_c is the center frequency, $\boldsymbol{e}(\cdot)$ is the unit direction vector, and $\langle\cdot,\cdot\rangle$ denotes the inner product. $\boldsymbol{\zeta}(\boldsymbol{f};\tau_l) \in \mathbb{C}^{1\times K}$ is the frequency response corresponding to the delay τ_l, with its k-th entry written as $\zeta(f_k;\tau_l) = \exp\{-j2\pi f_k \tau_l\}$.

The SAGE algorithm [38] is often used to estimate the parameters of MPCs. Its main advantage over conventional expectation-maximization (EM) algorithms is that a multi-dimensional search is replaced with several one-dimensional searches. Therefore, the computational complexity is significantly decreased, while the estimator still converges to the global maximum of its likelihood function with a sufficient number of iterations. A prerequisite to utilize the space-alternating mechanism is that the likelihood function needs to be independent between different parameter spaces [41]. This likelihood independency between direction $\boldsymbol{e}(\phi_l,\theta_l)$ and delay τ_l is guaranteed from the Kronecker structure of $\mathbf{H}(\boldsymbol{f};\tilde{\boldsymbol{\Theta}}_l)$ [39], as shown in (6). As a result, a sequentially parameter updating procedure, i.e. the space-alternating mechanism, can be deployed as in [38].

However, as discussed in the introduction, with the narrowband assumption violated, the Kronecker structure in (6) cannot be maintained due to the frequency dependency of $\boldsymbol{v}(\phi_l,\theta_l)$. Thus, the likelihood independency between $\boldsymbol{e}(\phi_l,\theta_l)$ and τ_l does not hold. Moreover, with the far-field assumption violated, an additional parameter, i.e. source distance $d_{0,l}$, is introduced in the signal model. Consequently, the sequentially parameter updating procedure cannot be applied between $\boldsymbol{e}(\phi_l,\theta_l)$, $d_{0,l}$ and τ_l for channels measured with wideband large-scale array systems. In other words, estimation needs to be done jointly among parameters in order to prevent the estimator from converging to a local maxima of the likelihood function. Fig. 2 gives the sketch of the feasibility region of the SAGE algorithm and the proposed algorithm with respect to array aperture and signal bandwidth.

IV. A Low-complexity Maximum Likelihood Estimator

Given the observation $\mathbf{Y}(\boldsymbol{f})$ at the output of the Rx array, the expectation of the log-likelihood function of the parameters

This article has been accepted for publication in a future issue of this journal, but has not been fully edited. Content may change prior to final publication. Citation information: DOI 10.1109/TWC.2018.2854553, IEEE Transactions on Wireless Communications

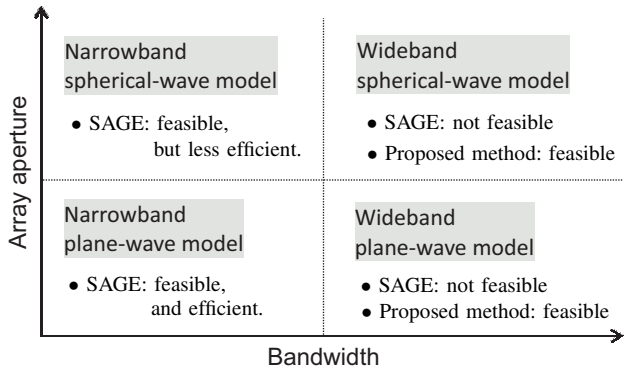

Fig. 2. Feasibility region of the SAGE and the proposed MLE algorithm.

$\boldsymbol{\Theta}$ can be written as [29]

$$\begin{aligned}&\mathrm{E}[\Lambda(\boldsymbol{\Theta};\mathbf{Y}(\boldsymbol{f}))] = \\ &-\ln(\pi\sigma_n^2) - \frac{1}{\sigma_n^2 MK}\left\|\mathrm{vec}\{\mathbf{Y}(\boldsymbol{f})\} - \mathrm{vec}\{\mathbf{H}(\boldsymbol{f};\boldsymbol{\Theta})\}\right\|^2,\end{aligned} \tag{8}$$

where $\mathrm{E}[\cdot]$ denotes expectation, and is calculated as the sample mean. The estimate of $\boldsymbol{\Theta}$ is obtained by maximizing (8) over the span of parameters,

$$\hat{\boldsymbol{\Theta}} = \arg\max_{\boldsymbol{\Theta}} \left\{\mathrm{E}[\Lambda(\boldsymbol{\Theta};\mathbf{Y}(\boldsymbol{f}))]\right\}. \tag{9}$$

A brute-force search for (9) is computationally prohibitive due to the high dimension of $\boldsymbol{\Theta}$ [38]. Given two paths, l and l', if any of the differences $|\phi_l - \phi_{l'}|$, $|\theta_l - \theta_{l'}|$, $|d_{0,l} - d_{0,l'}|$, and $|\tau_l - \tau_{l'}|$ is larger than the resolution in its respective domain, the inner product of $\mathrm{vec}\{\boldsymbol{s}(\boldsymbol{f};\boldsymbol{\Theta}_l^{\bar{\alpha}})\}$ and $\mathrm{vec}\{\boldsymbol{s}(\boldsymbol{f};\boldsymbol{\Theta}_{l'}^{\bar{\alpha}})\}$ approaches zero due to the orthogonality of their vector spaces [27], [38]. Therefore, $\hat{\boldsymbol{\Theta}}$ in (9) can be approximated alternatively through matched filtering [2], [38]. However, due to the large power difference between the strong MPCs and the weak MPCs, the mainlobes of the estimated power spectra of the weak MPCs may be buried under the sidelobes of the estimated power spectra of the strong MPCs, which causes interference to the estimation of the weak MPCs. To cope with that, the estimate $\hat{\boldsymbol{\Theta}}_l$ for individual paths can be obtained sequentially in a successive interference cancellation (SIC) manner as described below.

A. Procedure of an MLE Algorithm with SIC

The estimate $\hat{\boldsymbol{\Theta}}_l$ for individual paths can be obtained sequentially through the matched filtering with SIC as

$$\hat{\boldsymbol{\Theta}}_l^{\bar{\alpha}} = \arg\max_{\boldsymbol{\Theta}_l^{\bar{\alpha}}} \|z(\boldsymbol{\Theta}_l^{\bar{\alpha}})\|, \tag{10}$$

$$\hat{\alpha}_l = \frac{z(\hat{\boldsymbol{\Theta}}_l^{\bar{\alpha}})}{\|\mathrm{vec}\{\boldsymbol{s}(\boldsymbol{f};\hat{\boldsymbol{\Theta}}_l^{\bar{\alpha}})\}\|}, \tag{11}$$

where

$$z(\boldsymbol{\Theta}_l^{\bar{\alpha}}) = \frac{\mathrm{vec}\left\{\boldsymbol{s}(\boldsymbol{f};\boldsymbol{\Theta}_l^{\bar{\alpha}})\right\}^{\mathrm{H}}\mathrm{vec}\{\mathbf{Y}^{(l)}(\boldsymbol{f})\}}{\|\mathrm{vec}\{\boldsymbol{s}(\boldsymbol{f};\boldsymbol{\Theta}_l^{\bar{\alpha}})\}\|}, \tag{12}$$

and

$$\mathbf{Y}^{(l)}(\boldsymbol{f}) = \begin{cases}\mathbf{Y}(\boldsymbol{f}) & \text{if } l = 1.\\ \mathbf{Y}(\boldsymbol{f}) - \sum_{l'=1}^{l-1}\mathbf{H}(\boldsymbol{f};\hat{\boldsymbol{\Theta}}_{l'}) & \text{if } l > 1.\end{cases} \tag{13}$$

When the first path (i.e. $l = 1$) is estimated, the parameters are obtained with the original observation $\mathbf{Y}(\boldsymbol{f})$. The transfer function given in (1) is then reconstructed with respect to $\hat{\boldsymbol{\Theta}}_1$, and subtracted from the original observation $\mathbf{Y}(\boldsymbol{f})$. The remaining observation is then used for estimating the next path. This procedure is repeated until we have extracted a preset number of paths L, which is usually determined empirically.

B. A Coarse-to-Fine Search

The MLE is well-known for its high computational complexity due to its joint estimation mechanism, especially when the parameter dimension is large. The computational complexity comes from both the high-dimensional joint estimation and the large matrix size (i.e. $\mathbf{Y}(\boldsymbol{f}) \in \mathbb{C}^{M\times K}$) as well. In order to reduce the complexity, we separate the estimation for $\hat{\boldsymbol{\Theta}}_l$ into two stages, namely the initialization stage and the refinement stage.

1) The Initialization Stage: The frequency point with the highest signal power over M elements is selected as [32]

$$f_k^{max} = \arg\max_{f_k}\left\|\mathbf{Y}^{(l)}(f_k)\right\|^2, \tag{14}$$

where $\mathbf{Y}^{(l)}(f_k) \in \mathbb{C}^{M\times 1}$ is the k-th column vector of $\mathbf{Y}^{(l)}(\boldsymbol{f})$. The initial estimates of $\boldsymbol{\Theta}_l^{\bar{\alpha},\bar{\tau}} = \{\phi_l, \theta_l, d_{0,l}\}$ are obtained through the matched filtering as

$$(\hat{\boldsymbol{\Theta}}_l^{\bar{\alpha},\bar{\tau}})^{init} = \arg\max_{\boldsymbol{\Theta}_l^{\bar{\alpha},\bar{\tau}}}\left\|\underline{z}(f_k^{max};\boldsymbol{\Theta}_l^{\bar{\alpha},\bar{\tau}})\right\|, \tag{15}$$

where

$$\underline{z}(f_k;\boldsymbol{\Theta}_l^{\bar{\alpha},\bar{\tau}}) = \frac{\underline{\boldsymbol{s}}(f_k;\boldsymbol{\Theta}_l^{\bar{\alpha},\bar{\tau}})^{\mathrm{H}}\mathbf{Y}^{(l)}(f_k)}{\|\underline{\boldsymbol{s}}(f_k;\boldsymbol{\Theta}_l^{\bar{\alpha},\bar{\tau}})\|}, \tag{16}$$

and the m-th entry of $\underline{\boldsymbol{s}}(f_k;\boldsymbol{\Theta}_l^{\bar{\alpha},\bar{\tau}}) \in \mathbb{C}^{M\times 1}$ is

$$\begin{aligned}\underline{s}_m(f_k;\boldsymbol{\Theta}_l^{\bar{\alpha},\bar{\tau}}) =& \frac{g_m(f_k;\phi_l,\theta_l)}{4\pi f_k d_{m,l}/c}\\ &\cdot\exp\{-j2\pi f_k(d_{m,l} - d_{0,l})/c\}.\end{aligned} \tag{17}$$

The initial estimate of τ_l is then estimated following the same principle as

$$\hat{\tau}_l^{\,init} = \arg\max_{\tau_l}\frac{1}{\sqrt{K}}\left\|\sum_{k=1}^{K}\underline{z}\left(f_k;(\hat{\boldsymbol{\Theta}}_l^{\bar{\alpha},\bar{\tau}})^{init}\right)\exp\{j2\pi f_k\tau_l\}\right\|. \tag{18}$$

The initial estimates of $\boldsymbol{\Theta}_l^{\bar{\alpha}}$ are obtained as $(\hat{\boldsymbol{\Theta}}_l^{\bar{\alpha}})^{init} = \{\hat{\phi}_l^{init}, \hat{\theta}_l^{init}, \hat{d}_{0,l}^{init}, \hat{\tau}_l^{init}\}$.

This article has been accepted for publication in a future issue of this journal, but has not been fully edited. Content may change prior to final publication. Citation information: DOI 10.1109/TWC.2018.2854553, IEEE Transactions on Wireless Communications

2) The Refinement Stage: The search candidates are refined in the vicinity of the initial estimates $(\hat{\boldsymbol{\Theta}}_l^{\bar{\alpha}})^{init}$ obtained from the initialization stage. The MLE algorithm described in (10) to (13) is then conducted with the full observation matrix $\mathbf{Y}^{(l)}(\boldsymbol{f})$ over the confined region of the channel parameters to obtain the final estimates $\hat{\boldsymbol{\Theta}}_l$.

In the initialization stage, the matrix size decreases from $M \times K$ to $M \times 1$ and $1 \times K$ in (15) and (18), respectively. In the refinement stage, the number of search candidates is further decreased due to the confined region around the initial estimates. Therefore, the overall computational complexity decreases significantly.

C. Decision of Number of Paths $\hat{L}$

The number of paths $\hat{L}$ varies a lot with respect to different estimation algorithms. Usually, the maximum-likelihood based algorithms return more paths than the subspace-based algorithms. One of the reasons for this is that the MLE-based algorithms often assume specular propagation, so the diffuse scattering part of the channel would also be treated as specular paths, which could increase the number of paths drastically. Another reason is that when the deployed signal model does not match the measurement data, either due to a poor system calibration before measurement, or an invalid assumption (e.g. the narrowband or the far-field assumption) for a specific scenario, artificial paths would also be created during estimation. To alleviate over-estimation, the Akaike information criterion (AIC) [45]–[47] is used to determine the appropriate number of paths, and it can be expressed as

$$\mathrm{AIC}(L) = -2\Lambda(\hat{\Theta}) + \gamma L. \tag{19}$$

The first term stands for the likelihood as in (8), and the second term represents the penalty for overfitting. The factor γ can be adjusted to define different significance levels of the penalty [48]. By substituting (8) in (19), we obtain the AIC expression as

$$\mathrm{AIC}(L) = 2\ln(\pi\sigma_n^2) + \gamma L + \frac{2}{\sigma_n^2 MK}\left\|\mathrm{vec}\{\mathbf{Y}(\boldsymbol{f})\} - \mathrm{vec}\left\{\sum_{l=1}^{L}\mathbf{H}(\boldsymbol{f};\hat{\boldsymbol{\Theta}}_l)\right\}\right\|^2. \tag{20}$$

The appropriate number of paths is determined by $\hat{L} = \arg\min_L \mathrm{AIC}(L)$. Note the indices of the estimated paths need to be permuted according to the likelihood of each path calculated in (12) in descending order.

To have a more intuitive understanding for the decision $\hat{L}$ from (20), we calculate the first-order difference of $\mathrm{AIC}(L)$ as

$$\Delta\mathrm{AIC}(L) = \mathrm{AIC}(L) - \mathrm{AIC}(L-1), \tag{21}$$

where Δ denotes the difference operator. Inserting (20) into (21) yields

$$\Delta\mathrm{AIC}(L) = \frac{2}{\sigma_n^2 MK}\left\|\mathrm{vec}\{\mathbf{Y}(\boldsymbol{f})\} - \mathrm{vec}\left\{\sum_{l=1}^{L}\mathbf{H}(\boldsymbol{f};\hat{\boldsymbol{\Theta}}_l)\right\}\right\|^2 - \frac{2}{\sigma_n^2 MK}\left\|\mathrm{vec}\{\mathbf{Y}(\boldsymbol{f})\} - \mathrm{vec}\left\{\sum_{l=1}^{L-1}\mathbf{H}(\boldsymbol{f};\hat{\boldsymbol{\Theta}}_l)\right\}\right\|^2 + \gamma. \tag{22}$$

When the MPCs are well-separated in the parameter domain, $\mathrm{vec}\left\{\mathbf{H}(\boldsymbol{f};\hat{\boldsymbol{\Theta}}_l)\right\}$ is roughly orthogonal to $\mathrm{vec}\left\{\mathbf{H}(\boldsymbol{f};\hat{\boldsymbol{\Theta}}_{l'})\right\}$ given $l \neq l'$. By applying the Pythagorean theorem, (22) can be approximated as

$$\Delta\mathrm{AIC}(L) = -\frac{2}{\sigma_n^2 MK}\left\|\mathrm{vec}\left\{\mathbf{H}(\boldsymbol{f};\hat{\boldsymbol{\Theta}}_L)\right\}\right\|^2 + \gamma. \tag{23}$$

Since the indices of the estimated paths are permuted in descending order of the likelihood, the term $\left\|\mathrm{vec}\left\{\mathbf{H}(\boldsymbol{f};\hat{\boldsymbol{\Theta}}_L)\right\}\right\|^2$, which can be interpreted as the power of the L-th path, decreases monotonically with L. In other words, the first-order difference of $\mathrm{AIC}(L)$ increases monotonically with L, and hence the second-order difference of $\mathrm{AIC}(L)$ is non-negative. Therefore, $\mathrm{AIC}(L)$ is convex, and its minimum can be achieved when $\Delta\mathrm{AIC}(L) = 0$ [49]. Setting (23) to zero leads to

$$\frac{1}{\sigma_n^2 MK}\left\|\mathrm{vec}\left\{\mathbf{H}(\boldsymbol{f};\hat{\boldsymbol{\Theta}}_L)\right\}\right\|^2 = \frac{\gamma}{2}, \tag{24}$$

which indicates this criterion can be interpreted as a threshold in power-to-noise ratio averaged by MK. The estimated paths with power-to-noise ratio above $\gamma/2$ will be considered as dominant and kept. $\gamma = 2$ was assumed to be sufficient in significance in [45]. When $\gamma = 2$ is used, it corresponds to a power-to-noise ratio of $0\,\mathrm{dB}$. In the following sections, $\gamma = 2$ was also used for data processing. The whole procedure of the proposed MLE algorithm is summarized in Algorithm 1.

Algorithm 1 Procedure of the proposed MLE algorithm with SIC.

Input: $\mathbf{Y}(\boldsymbol{f}), L$
  for $l = 1$ **to** L **do**
    Initialization:
      $(\hat{\boldsymbol{\Theta}}_l^{\bar{\alpha}})^{init} = \{\hat{\phi}_l^{init}, \hat{\theta}_l^{init}, \hat{d}_{0,l}^{init}, \hat{\tau}_l^{init}\}$. // Eqs. (14) to (18)
      Define search candidates with respect to $(\hat{\boldsymbol{\Theta}}_l^{\bar{\alpha}})^{init}$.
    Refinement:
      $\hat{\boldsymbol{\Theta}}_l = \{\hat{\alpha}_l, \hat{\phi}_l, \hat{\theta}_l, \hat{d}_{0,l}, \hat{\tau}_l\}$. // Eqs. (10) to (12)
    SIC:
      $\mathbf{Y}^{(l)}(\boldsymbol{f})$. // (13)
  end for
  Rearrange path indices with respect to likelihood in descending order. // (12)
  Determine $\hat{L}$ with AIC. // (20)
Output: $\hat{\boldsymbol{\Theta}} = \{\hat{\boldsymbol{\Theta}}_1, \hat{\boldsymbol{\Theta}}_2, \ldots, \hat{\boldsymbol{\Theta}}_{\hat{L}}\}$.

V. Channel Measurement and Estimation

A. Indoor LoS and OLoS Scenarios

The measurements were conducted in a basement. A sketch of the measurement area is shown in Fig. 3(a). Two sets of antenna configurations were used in the measurements, namely "Config. 1" and "Config. 2". For "Config. 1", both the Tx and the Rx were equipped with biconical antennas. For "Config. 2", the Rx antenna was replaced with a horn antenna. The antenna specifications are summarized in Table I.

This article has been accepted for publication in a future issue of this journal, but has not been fully edited. Content may change prior to final publication. Citation information: DOI 10.1109/TWC.2018.2854553, IEEE Transactions on Wireless Communications

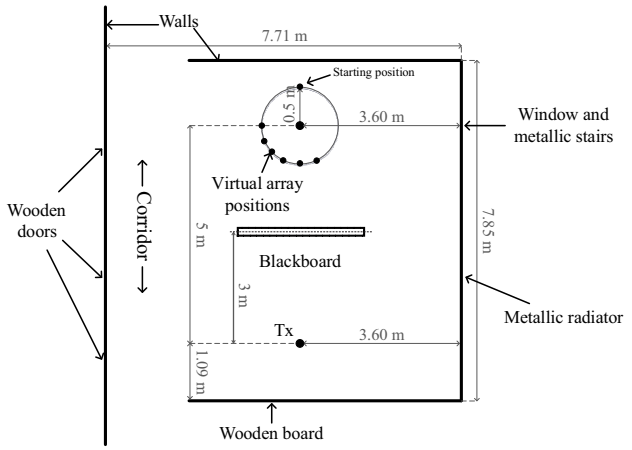

(a)

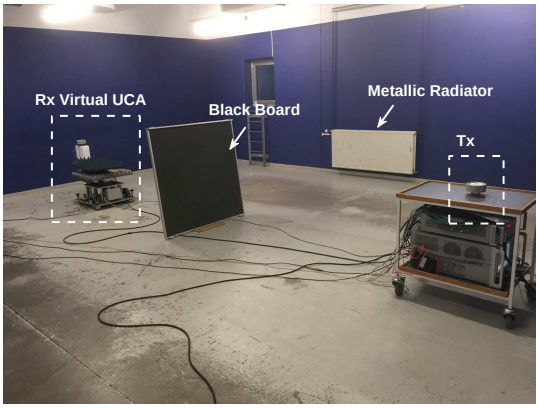

(b)

Fig. 3. (a) Dimensions and (b) photo of the measurement environment.

During the measurement, both the Tx and the Rx antenna were placed $0.84\,\mathrm{m}$ above the floor. The Rx antenna was mounted on a turntable. A virtual UCA of 720 elements, i.e. $M = 720$, with radius $0.5\,\mathrm{m}$ was formed on the Rx side. The frequency response was measured with a VNA from 28-30 GHz with 750 frequency points, i.e. $K = 750$, at each element position. The corresponding delay range is $[0,\ 374.5]\,\mathrm{ns}$. The inter-element spacing of the UCA is $4.4\,\mathrm{mm}$, which is smaller than half the wavelength at 30 GHz (i.e. $5\,\mathrm{mm}$). Therefore, spatial aliasing is avoided [50]. The Fraunhofer distance at 30 GHz is $200\,\mathrm{m}$, whereas the distance between the Tx and the center of the Rx array is only $5\,\mathrm{m}$ (see Fig. 3(a)). Thus, the far-field assumption is not met in our measurement. The narrowband assumption does not hold either since the array aperture (i.e. $1\,\mathrm{m}$) is much larger than the delay resolution multiplied by the speed of light (i.e. $0.15\,\mathrm{m}$). The measurement settings are summarized in Table I.

Note that in "Config. 2", when the horn antenna was deployed at the Rx, the feed of the horn was positioned at the rotation center of the turntable. Therefore, the rotation radius is denoted as $0\,\mathrm{m}$ in Table I. Also note that to cope with the influence of the cable effect in the measurement setup, the RF cable was fixed to a wooden board to minimize the cable movement.

For each set of antenna configurations, two scenarios were considered, i.e. the line-of-sight (LoS) and the obstructed line-of-sight (OLoS) scenario. The OLoS scenario was created by placing an additional blackboard with a metallic substrate of dimensions $1.19\,\mathrm{m} \times 1.19\,\mathrm{m}$ between the Tx and the Rx to block the LoS path. When measuring the LoS scenario, the blackboard was removed from the environment. A photo of the measurement environment is shown in Fig. 3(b). Readers are referred to [16] for a full description of the measurement campaign.

The rotational horn antenna measurement was conducted to obtain a reference PADP of the channel. The estimated PADP from the UCA measurement are compared to the reference PADP to assess the performance of the proposed algorithm in the next subsection.

TABLE I
ANTENNA SPECIFICATIONS AND MEASUREMENT SETTINGS.

Antenna specifications		
	Horn	Biconical
Operating frequency	26.4-40.1 GHz	2-30 GHz
Half-power beamwidth[a]	20°	Omnidirectional
Gain[b]	19 dB	6 dB
Polarization	Vertical	Vertical
Measurement settings		
	Config. 1	Config. 2
Tx antenna	Biconical	Biconical
Rx antenna	Biconical	Horn
Rx rotation radius	0.5 m	0 m
Azimuth rotation span	0°-360° with 720 steps	
Frequency sweep range	28-30 GHz with 750 points	

[a]Evaluated in the azimuth plane at 28-30 GHz.
[b]Evaluated at 28-30 GHz.

B. MPC Parameter Estimation and Comparison between the SWM and the PWM

According to the data sheet of the biconical antenna [51], the variation of the antenna gain in the measurement frequency range is up to $1.5\,\mathrm{dB}$, so we assume frequency independent antenna response for the estimation. The measurement data were processed with the proposed algorithm based on the SWM and the PWM, respectively. Initially, 60 paths were assigned to the estimator for both the LoS and the OLoS scenario. Fig. 4 shows the likelihood function and the AIC with respect to the number of paths for both scenarios. It can be clearly seen that the likelihood obtained with the SWM is always higher than that obtained with the PWM for both scenarios. Also, the AIC of the SWM is always lower than that of the PWM. Therefore, it can be concluded that the SWM is superior to the PWM for the large-scale antenna array systems in the estimation.

Moreover, the likelihood for the SWM increases significantly with the number of paths at first. After a certain point, it tends to converge for both scenarios, which means

This article has been accepted for publication in a future issue of this journal, but has not been fully edited. Content may change prior to final publication. Citation information: DOI 10.1109/TWC.2018.2854553, IEEE Transactions on Wireless Communications

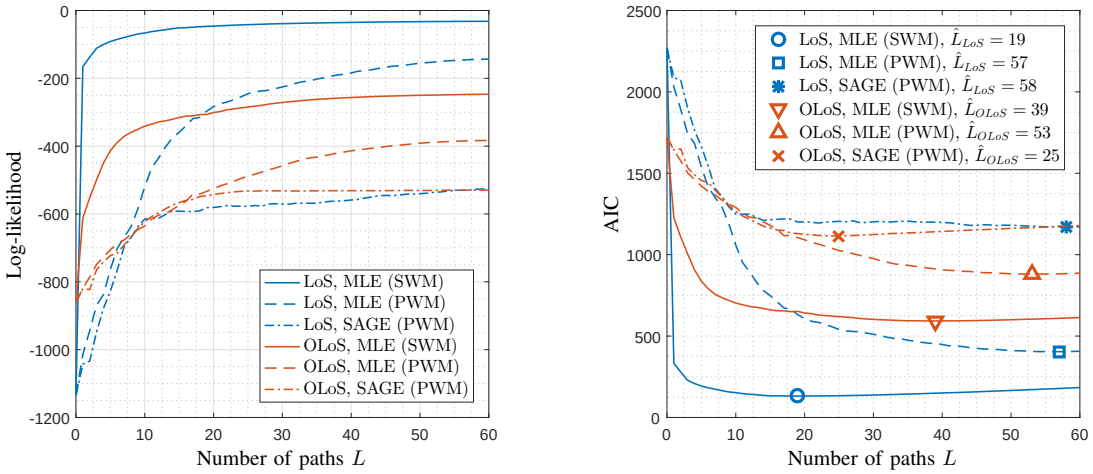

Fig. 4. The log-likelihood (left) and the AIC (right) with respect to the number of paths for the LoS and the OLoS scenario. Results from the SAGE algorithm based on the PWM with 10 EM iterations are also presented for comparison.

the additional benefits of using a larger number of paths are insignificant. The number of paths is selected at the minimum AIC, which corresponds to $\hat{L}_{\mathrm{LoS}} = 19$ and $\hat{L}_{\mathrm{OLoS}} = 39$ for the LoS and the OLoS scenario, respectively. The number of paths for the PWM is $\hat{L}_{\mathrm{LoS}} = 57$ and $\hat{L}_{\mathrm{OLoS}} = 53$. By comparison, both a higher likelihood and a less number of paths are obtained with the SWM, which shows the advantages of the SWM for large-scale array systems. The results obtained from the SAGE algorithm based on the PWM with 10 EM iterations are also given in Fig. 4, which shows it does not work well for wideband signals. Estimation with the SAGE algorithm assuming the SWM were not carried out due to its high computation time caused by the joint estimation together with multiple iterations of calculation.

Fig. 5 and Fig. 6 show the estimated PADP in comparison to that measured with the horn antenna for the LoS and the OLoS scenario, respectively. For the LoS scenario in Fig. 5, it can be observed that the resulting PADP from the SWM matches that from the horn measurement very well, whereas using the PWM leads to poor extraction of the weak paths even with a larger number of paths. Moreover, most of the MPCs (i.e. 49 out of 57) estimated with the PWM concentrate in the region around the LoS component, which shows a severe model mismatch between the PWM and the measurement. This is due to the fact that the power of the LoS component is dominant, and it would be estimated first by the estimator. However, if the transfer function reconstructed form the signal model is not accurate enough to cancel its contribution in the observation $\mathbf{Y}(\boldsymbol{f})$, artificial paths would be recursively created and estimated around the LoS component due to the incomplete cancellation. In addition, there is an obvious difference in power between the dominant MPCs estimated from the SWM and the PWM. For example, the power of the LoS component for the SWM case is around 10 dB higher than that for the PWM case. The power loss from the PWM was also reported in [26], [27], which is considered as a result of the model mismatch in near-field estimation problems.

For the OLoS scenario in Fig. 6, the PADP from the PWM

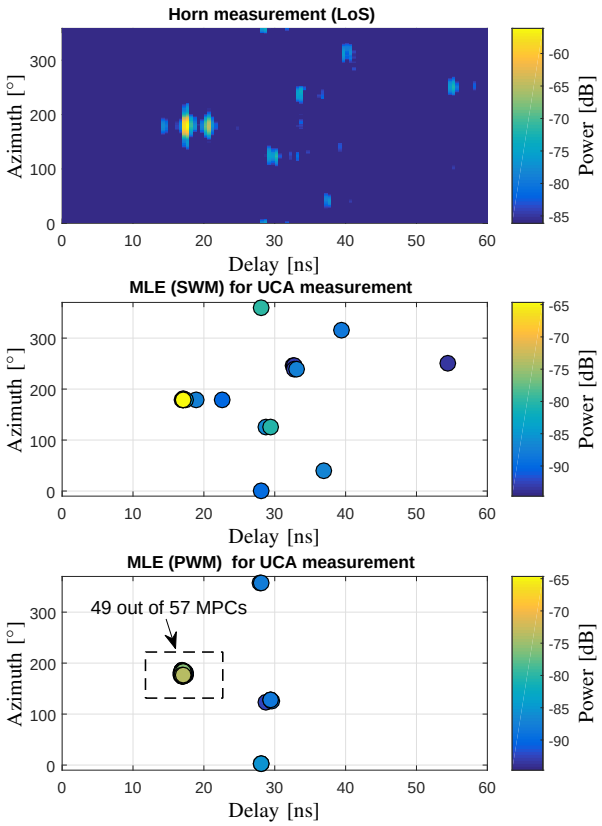

Fig. 5. The reference PADP obtained from the horn measurement (top) and the estimated MPCs for the LoS scenario. 19 paths are shown for the SWM (middle), and 57 paths for the PWM (bottom) according to the number of paths set by the AIC criterion as shown in Fig. 4.

is more similar to that from the SWM compared to the LoS scenario. This is due to the fact that the power of the MPCs is more evenly distributed for the OLoS scenario. However, model mismatch can still be observed from the difference in power between the MPCs estimated with the PWM and those with the SWM. According to the observations from Figs. 4 to 6, it can be concluded that the SWM outperforms the PWM

This article has been accepted for publication in a future issue of this journal, but has not been fully edited. Content may change prior to final publication. Citation information: DOI 10.1109/TWC.2018.2854553, IEEE Transactions on Wireless Communications

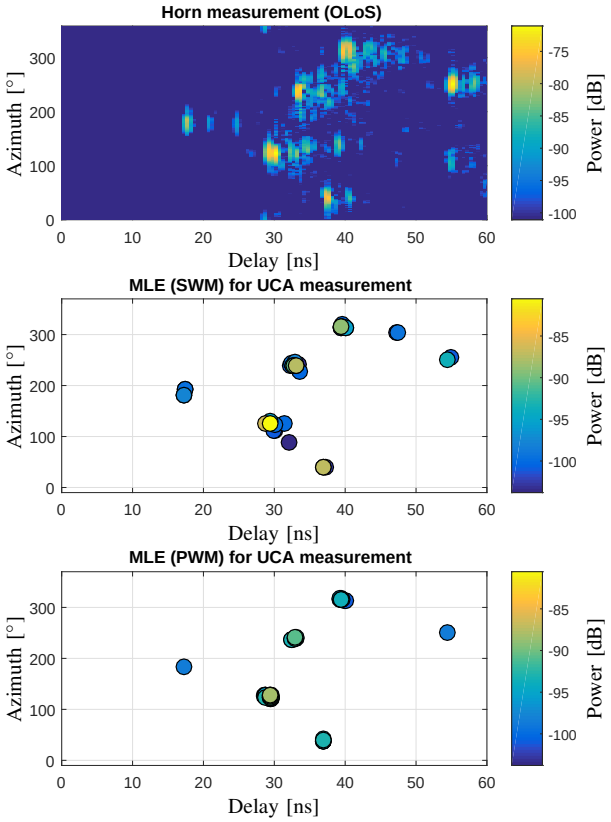

Fig. 6. The reference PADP obtained from the horn measurement (top) and the estimated MPCs for the OLoS scenario. 39 paths are shown for the SWM (middle), and 53 paths for the PWM (bottom) according to the number of paths set by the AIC criterion as shown in Fig. 4.

for near-field estimation problems. It is worth mentioning that a clustering procedure [52] can be applied to the estimated MPCs for cluster based channel models [23].

C. Power Delay Profile and Power Extraction Rate

The power delay profile (PDP) for each element of the array is calculated as the inverse discrete Fourier transform (IDFT) of the reconstructed channel frequency response using the SWM for the LoS and the OLoS scenario, as shown in Fig. 7 and Fig. 8, respectively. A good match between them can be clearly seen. The power extraction rate $\hat{P}$ is further calculated as

$$\hat{P} = 1 - \frac{\left\| \mathrm{vec}\left\{ \mathbf{H}(\boldsymbol{f}; \hat{\boldsymbol{\Theta}}) - \mathbf{Y}(\boldsymbol{f}) \right\} \right\|^2}{\left\| \mathrm{vec}\left\{ \mathbf{Y}(\boldsymbol{f}) \right\} \right\|^2}. \tag{25}$$

$\hat{P}_{\mathrm{LoS}} = 95\%$ and $\hat{P}_{\mathrm{OLoS}} = 69\%$ are obtained for the SWM case for the LoS and the OLoS scenario, respectively. In comparison, a lower power extraction rate of $\hat{P}_{\mathrm{LoS}} = 86\%$ and $\hat{P}_{\mathrm{OLoS}} = 54\%$ are obtained for the PWM case. For the LoS scenario, the LoS component is the main contribution of the total power, hence the high extraction rate. For the OLoS scenario, the proportion of the power in the diffuse scattering components becomes more significant as seen in the background in Fig. 8, and a lower extraction rate is expected.

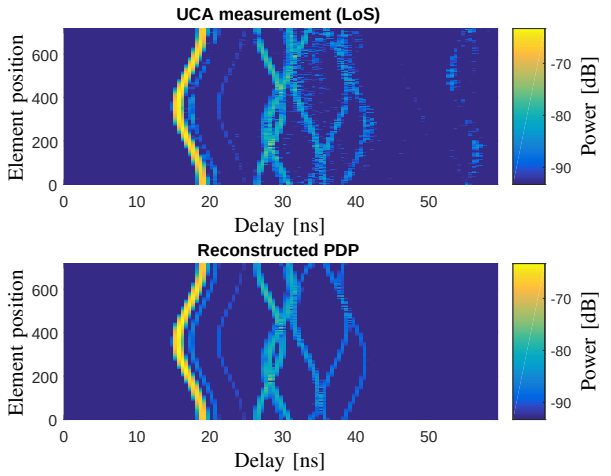

Fig. 7. The PDP of all elements from measurement (top), and the reconstructed channel (bottom) with the SWM for the LoS scenario with 30 dB power range.

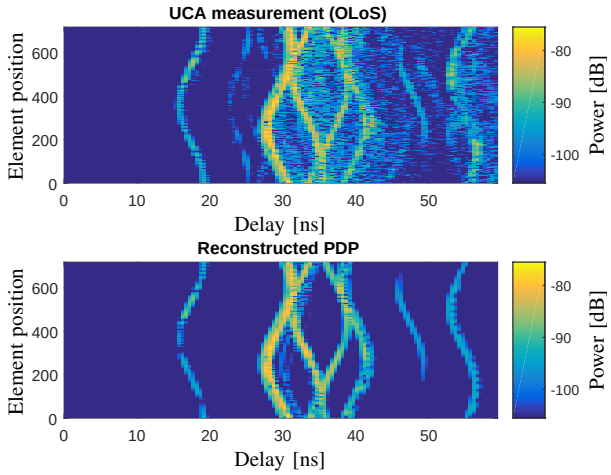

Fig. 8. The PDP of all elements from measurement (top), and the reconstructed channel (bottom) with the SWM for the OLoS scenario with 30 dB power range.

D. Channel Characteristics Obtained from Estimated MPCs

Channel characteristics including azimuth spread of arrival (ASA), elevation spread of arrival (ESA), and delay spread (DS), are calculated the same way as in [23], and are listed in Table II. Huge differences can be seen between the parameter spreads obtained from the proposed MLE algorithm with the PWM and the SWM. For example, the DS and the ASA from the SWM results are much larger than those from the PWM results, whereas the ESA for the LoS scenario from the SWM results is only around one-fourth of that from the PWM results. This is because the estimator implemented with the SWM captured more weak MPCs, which are widely spread in the azimuth and delay domain. In contrast, the estimator implemented with the PWM returned many artificial paths around the dominant paths due to the model mismatch, which causes spread in the elevation domain. The comparison shows the model mismatch can severely affect the estimated channel characteristics. The corresponding values given in 3GPP

This article has been accepted for publication in a future issue of this journal, but has not been fully edited. Content may change prior to final publication. Citation information: DOI 10.1109/TWC.2018.2854553, IEEE Transactions on Wireless Communications

TABLE II
CHANNEL CHARACTERISTICS OBTAINED FROM MLE (PWM), MLE (SWM), AND 3GPP FOR INDOOR SCENARIOS AT 28-30 GHz.

Characteristics	MLE (PWM)		MLE (SWM)		3GPP[a]	
	LoS	OLoS	LoS	OLoS	LoS	NLoS
DS [ns]	2.14	4.24	3.82	5.55	19.64	25.90
ASA [°]	18.58	74.01	24.96	81.15	31.65	50.18
ESA [°]	4.64	3.76	0.92	2.20	11.37	14.64

[a]The values are evaluated at 29 GHz with respect to the indoor-office scenarios in 3GPP TR 38.901 [23]. NLoS denotes non-LoS scenarios.

TR 38.901 for the indoor-office scenario are also presented. Basically, the values from TR 38.901 are several times larger than those from the SWM, except the ASA for the non-line-of-sight (NLoS) scenarios. Since the parameter values from our measurement are obtained in a specific environment, they are not necessarily very representative. However, it has been extensively discussed in recent meetings, e.g. IRACON [53], that the parameter values in the current release of 3GPP model for high frequency bands may also be changed in future due to the lack of input from measurement data.

E. Physical Interpretation of the Estimated MPCs

In order to have a physical interpretation of the propagation mechanism, the estimated propagation paths are usually traced back in the physical environment [54]–[56]. A simple ray tracer is used here [44]. For a LoS path or a one-bounce path, a unique path can be drawn in physical environment through simple geometry with the delay and the direction of arrival information. For multi-bounce paths, since we only have the path parameters estimated from the Rx side, it is unknown if they are induced from either reflection or diffraction, or a combination of both. Here we assume only specular reflection for high-order bounces (i.e. second-order and above). The estimated paths are traced in the environment for both the LoS and the OLoS scenario as shown in Fig. 9. Moreover, it is interesting to see if the estimated locations of the scatterers can match any physical object in the environment. Thus, the locations of scatterers are also plotted as solid circles in Fig. 9. The location of the scatterer associated with the l-th path is calculated as the point from where the distance to the Rx array center along the path trajectory is equal to $\hat{d}_{0,l}$. The color shows the power of each path.

Fig. 9(a) shows the path trajectories for the LoS scenario. Due to the metallic radiator (heater) on the right wall, it can be seen the power reflected from the right wall is higher than that from the left wall. From the estimated scatterer locations, it can be observed that some of them are traced back to the the Tx location, whereas the others are a bit off the physical objects, which can be induced from the insufficient modelling of the environment. In addition, since the estimation for the distance d_0 relies on the curvature of the spherical wavefront impinging upon the array, the estimation for a farther scattering source would be less accurate.

Fig. 9(b) shows the path trajectories for the OLoS scenario. It can be observed that the power of the LoS component is significantly attenuated by the blackboard. Besides the reflection from the walls, the diffraction from the edges of the blackboard can be seen as well. Most of the estimated scatterer locations are either close to the walls, the edges of the blackboard, or the Tx. The good match between the estimated scatterer locations and the physical objects helps to reveal the propagation mechanisms like reflection and diffraction. Nonetheless, it is worth noting that when the surfaces of the interacting objects are large and flat, e.g. walls, the shape of the spherical wavefront is preserved after reflection, so the scattering sources would be traced back to the Tx location, as shown with some two-bounce paths in Fig. 9.

VI. CONCLUSION

In this paper, an MLE algorithm with SIC is proposed for channel estimation when both the far-field and the narrowband assumptions are violated. The wideband SWM is used as the generic signal model for estimation. To reduce the computational complexity of traditional MLE algorithms, a two-stage procedure is introduced, which consists of an initialization stage and an estimation refinement stage. To alleviate over-estimation of the channel, the AIC is used to determine the appropriate number of paths in the channel.

The proposed algorithm is applied to estimate parameters of the channel measured with a large-scale antenna array system in a basement at 28-30 GHz, including a LoS and an OLoS scenario. It is shown that for near-field estimation problems, the SWM outperforms the PWM significantly in terms of likelihood, number of paths estimated, and power extraction rate. By comparing the estimated PADP from the UCA measurement to that from a rotational horn antenna measurement, it is shown that the majority of channel components are successfully captured.

Moreover, the physical interpretation of the propagation channel is given along with the environment. The estimated scatterer locations are observed to coincide with the physical objects in the environment, such as the walls, the edges of the blackboard, and the Tx. It is observed that reflection does not always create new scattering sources on the interacting objects. This is due to the fact that the original spherical wavefront is preserved after reflection given that the surface of the interacting objects is sufficiently large and flat, e.g. walls. As a result, the scattering sources are traced back to the Tx location for multi-bounce links.

Last but not least, the proposed low-complexity MLE algorithm could be useful for extracting channel parameters for standard channel models (e.g. 3GPP channel model) with the SWM taken into account. Extension on the algorithm for dual-polarization estimation will be conducted in future work. The findings on the propagation mechanisms and the obtained channel characteristics at 28-30 GHz would be helpful for channel characterization at high frequency bands.

REFERENCES

[1] F. Rusek, D. Persson, B. K. Lau, E. G. Larsson, T. L. Marzetta, O. Edfors, and F. Tufvesson, "Scaling Up MIMO: Opportunities and Challenges with Very Large Arrays," *IEEE Signal Processing Magazine*, vol. 30, no. 1, pp. 40–60, 2013.

[2] D. Tse and P. Viswanath, *Fundamentals of wireless communication*. Cambridge university press, 2005.

This article has been accepted for publication in a future issue of this journal, but has not been fully edited. Content may change prior to final publication. Citation information: DOI 10.1109/TWC.2018.2854553, IEEE Transactions on Wireless Communications

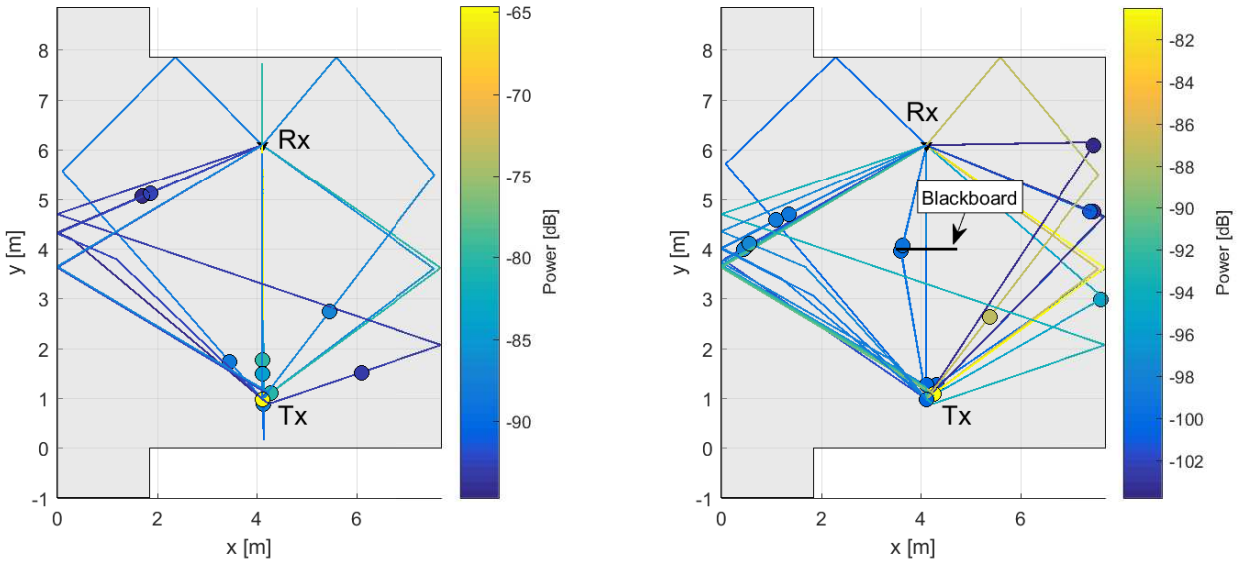

(a) LoS scenario (b) OLoS scenario

Fig. 9. The propagation paths trajectories in the physical environment for the LoS and the OLoS scenario. Scattering sources are plotted along the path trajectories in solid circles. The color shows the power in dB.

[3] J. Kivinen, "60-GHz Wideband Radio Channel Sounder," *IEEE Transactions on Instrumentation and Measurement*, vol. 56, no. 5, pp. 1831–1838, 2007.

[4] W. Zhu and H. Kong, "mmWave MIMO channel sounding for 5G," in *1st International Conference on 5G for Ubiquitous Connectivity*, 2014, pp. 192–197.

[5] R. Müller, R. Herrmann, D. A. Dupleich, C. Schneider, and R. S. Thomä, "Ultrawideband Multichannel Sounding for mm-Wave," in *The 8th European Conference on Antennas and Propagation (EuCAP 2014)*, 2014, pp. 817–821.

[6] X. Gao, O. Edfors, F. Rusek, and F. Tufvesson, "Massive MIMO Performance Evaluation Based on Measured Propagation Data," *IEEE Transactions on Wireless Communications*, vol. 14, no. 7, pp. 3899–3911, 2015.

[7] V. Kristem, S. Sangodoyin, C. U. Bas, M. Käske, J. Lee, C. Schneider, G. Sommerkorn, J. Zhang, R. S. Thomä, and A. F. Molisch, "3D MIMO Outdoor-to-Indoor Propagation Channel Measurement," *IEEE Transactions on Wireless Communications*, vol. 16, no. 7, pp. 4600–4613, 2017.

[8] À. O. Martínez, E. De Carvalho, and J. Ø. Nielsen, "Massive MIMO properties based on measured channels: Channel hardening, user decorrelation and channel sparsity," in *2016 50th Asilomar Conference on Signals, Systems and Computers*, 2016, pp. 1804–1808.

[9] B. Ai, K. Guan, R. He, J. Li, G. Li, D. He, Z. Zhong, and K. M. S. Huq, "On Indoor Millimeter Wave Massive MIMO Channels: Measurement and Simulation," *IEEE Journal on Selected Areas in Communications*, vol. 35, no. 7, pp. 1678–1690, 2017.

[10] J. Hejselbaek, W. Fan, and G. F. Pedersen, "Ultrawideband VNA based channel sounding system for centimetre and millimetre wave bands," in *IEEE International Symposium on Personal, Indoor and Mobile Radio Communications, PIMRC*, 2016, pp. 1–6.

[11] S. Salous, S. M. Feeney, X. Raimundo, and A. A. Cheema, "Wideband MIMO Channel Sounder for Radio Measurements in the 60 GHz Band," *IEEE Transactions on Wireless Communications*, vol. 15, no. 4, pp. 2825–2832, 2016.

[12] B. Ai, X. Cheng, T. Kurner, Z. D. Zhong, K. Guan, R. S. He, L. Xiong, D. W. Matolak, D. G. Michelson, and C. Briso-Rodriguez, "Challenges toward wireless communications for high-speed railway," *IEEE Transactions on Intelligent Transportation Systems*, vol. 15, no. 5, pp. 2143–2158, 2014.

[13] R. He, O. Renaudin, V. M. Kolmonen, K. Haneda, Z. Zhong, B. Ai, S. Hubert, and C. Oestges, "Vehicle-to-Vehicle Radio Channel Characterization in Crossroad Scenarios," *IEEE Transactions on Vehicular Technology*, vol. 65, no. 8, pp. 5850–5861, 2016.

[14] K. Haneda, J. Järveläinen, A. Karttunen, M. Kyrö, and J. Putkonen, "A statistical spatio-temporal radio channel model for large indoor environments at 60 and 70 GHz," *IEEE Transactions on Antennas and Propagation*, vol. 63, no. 6, pp. 2694–2704, 2015.

[15] J. Chen, X. Yin, X. Cai, and S. Wang, "Measurement-Based Massive MIMO Channel Modeling for Outdoor LoS and NLoS Environments," *IEEE Access*, vol. 5, pp. 2126–2140, 2017.

[16] W. Fan, I. Carton, J. Nielsen, K. Olesen, and G. F. Pedersen, "Measured wideband characteristics of indoor channels at centimetric and millimetric bands," *Eurasip Journal on Wireless Communications and Networking*, vol. 2016, no. 1, pp. 1–13, 2016.

[17] C. A. Balanis, *Antenna Theory: Analysis and Design*. John Wiley & Sons, 2005.

[18] A. J. Weiss and B. Friedlander, "Range and Bearing Estimation Using Polynomial Rooting," *IEEE Journal of Oceanic Engineering*, vol. 18, no. 2, pp. 130–137, 1993.

[19] C. Capps, "Near field or far field?" *EDN Magazine*, vol. 46, no. 18, pp. 95–102, 2001.

[20] L. Liu, D. W. Matolak, C. Tao, Y. Lu, and H. Chen, "Far region boundary definition of linear massive MIMO antenna arrays," in *2015 IEEE 82nd Vehicular Technology Conference (VTC2015-Fall)*, 2015, pp. 1–6.

[21] M. Fresia, M. Honglei, and J. Luo, "Use case characterization KPIs and preferred suitable frequency ranges for future 5G systems between 6 GHz and 100 GHz," Deliverable D1.1, the mmMAGIC project, Tech. Rep., 2015.

[22] A. Maltsev, A. Pudeyev, I. Bolotin, G. Morozov, K. Ingolf, M. Faerber, I. Siaud, A.-M. Ulmer-Moll, J.-M. Conrat, R. J. Weiler, M. Peter, and W. Keusgen, "Channel Modeling and Characterization," Deliverable FP7-ICT 368721/D5.1, MiWEBA, Tech. Rep., 2014.

[23] 3GPP, "Study on channel model for frequencies from 0.5 to 100 GHz," Tech. Rep. 3GPP TR 38.901 V14.0.0, 2017. [Online]. Available: http://www.etsi.org/standards-search

[24] K. Haneda, J. Zhang, L. Tan, G. Liu, Y. Zheng, H. Asplund, J. Li, Y. Wang, D. Steer, C. Li, T. Balercia, S. Lee, Y. Kim, A. Ghosh, T. Thomas, T. Nakamura, Y. Kakishima, T. Imai, H. Papadopoulos, T. S. Rappaport, G. R. Maccartney, M. K. Samimi, S. Sun, O. Koymen, S. Hur, J. Park, C. Zhang, E. Mellios, A. F. Molisch, S. S. Ghassamzadeh, and A. Ghosh, "5G 3GPP-like channel models for outdoor urban microcellular and macrocellular environments," in *2016 IEEE 83rd Vehicular Technology Conference (VTC Spring)*, 2016, pp. 1–7.

[25] C. F. Lopez, C. X. Wang, and R. Feng, "A novel 2D non-stationary wideband massive MIMO channel model," in *2016 IEEE 21st International Workshop on Computer Aided Modelling and Design of Communication Links and Networks (CAMAD)*, 2016, pp. 207–212.

[26] K. Haneda, J. I. Takada, and T. Kobayashi, "A parametric UWB propagation channel estimation and its performance validation in an anechoic chamber," *IEEE Transactions on Microwave Theory and Techniques*, vol. 54, no. 4, pp. 1802–1811, 2006.

[27] Y. Ji, W. Fan, and G. F. Pedersen, "Near-Field Signal Model for Large-Scale Uniform Circular Array and Its Experimental Validation," *IEEE Antennas and Wireless Propagation Letters*, vol. 16, pp. 1237–1240, 2017.

[28] X. Yin, S. Wang, N. Zhang, L. Tian, and B. Ai, "Scatterer Localization using Large-scale Antenna Arrays based on A Spherical Wavefront Parametric Model," *IEEE Transactions on Wireless Communications*, vol. 16, no. 10, pp. 6543–6556, 2017.

[29] H. Krim and M. Viberg, "Two decades of array signal processing research: The parametric approach," *IEEE Signal Processing Magazine*, vol. 13, no. 4, pp. 67–94, 1996.

[30] A. F. Molisch, "Ultrawideband propagation channels-theory, measurement, and modeling," *IEEE Transactions on Vehicular Technology*, vol. 54, no. 5, pp. 1528–1545, 2005.

[31] A. B. Baggeroer, W. A. Kuperman, and H. Schmidt, "Matched field processing: Source localization in correlated noise as an optimum parameter estimation problem," *The Journal of the Acoustical Society of America*, vol. 83, no. 2, pp. 571–587, 1988.

[32] J. A. Cadzow, "Multiple source location: The signal subspace approach," in *Twenty-Third Asilomar Conference on Signals Systems and Computers 1989*, vol. 2, no. 7, 1989, pp. 1110–1125.

[33] T. Tung, K. Yao, D. Chen, R. Hudson, and C. Reed, "Source localization and spatial filtering using wideband MUSIC and maximum power beamforming for multimedia applications," in *1999 IEEE Workshop on Signal Processing Systems. SiPS 99. Design and Implementation (Cat. No.99TH8461)*, 1999, pp. 625–634.

[34] Y. Wang, J. Li, P. Stoica, M. Sheplak, and T. Nishida, "Wideband RELAX and wideband CLEAN for aeroacoustic imaging," *The Journal of the Acoustical Society of America*, vol. 115, no. 2, pp. 757–767, 2004.

[35] R. Schmidt, "Multiple emitter location and signal parameter estimation," *IEEE Transactions on Antennas and Propagation*, vol. 34, no. 3, pp. 276–280, 1986.

[36] R. Roy and T. Kailath, "ESPRIT-Estimation of Signal Parameters Via Rotational Invariance Techniques," *IEEE Transactions on Acoustics, Speech, and Signal Processing*, vol. 37, no. 7, pp. 984–995, 1989.

[37] T. Hirano and N. Kikuma, "Location Estimation of Multiple Near-Field Broadband Sources by Combined Use of DOA-Matrix Method and SAGE Algorithm in Array Antenna Processing," in *2012 International Symposium on Antennas and Propagation (ISAP)*, 2012, pp. 363–366.

[38] B. H. Fleury, M. Tschudin, R. Heddergott, D. Dahlhaus, and K. I. Pedersen, "Channel parameter estimation in mobile radio environments using the SAGE algorithm," *IEEE Journal on Selected Areas in Communications*, vol. 17, no. 3, pp. 434–450, 1999.

[39] A. Richter, "Estimation of Radio Channel Parameters : Models and Algorithms," Ph.D. dissertation, 2005.

[40] J. Chen, S. Wang, and X. Yin, "A Spherical-Wavefront-Based Scatterer Localization Algorithm Using Large-Scale Antenna Arrays," *IEEE Communications Letters*, vol. 20, no. 9, pp. 1796–1799, 2016.

[41] J. A. Fessler and A. O. Hero, "Space-Alternating Generalized Expectation-Maximization Algorithm," *IEEE Transactions on Signal Processing*, vol. 42, no. 10, pp. 2664–2677, 1994.

[42] Y. Yu, H. S. Lui, C. H. Niow, and H. T. Hui, "Improved DOA estimations using the receiving mutual impedances for mutual coupling compensation: An experimental study," *IEEE Transactions on Wireless Communications*, vol. 10, no. 7, pp. 2228–2233, 2011.

[43] F. Zhang, W. Fan, and G. F. Pedersen, "Frequency-Invariant Uniform Circular Array for Wideband mm-Wave Channel Characterization," *IEEE Antennas and Wireless Propagation Letters*, vol. 16, pp. 641–644, 2017.

[44] Y. Ji, W. Fan, and G. F. Pedersen, "Channel estimation using spherical-wave model for indoor LoS and obstructed LoS scenarios," in *2017 11th European Conference on Antennas and Propagation, EUCAP 2017*, 2017, pp. 2459–2462.

[45] H. Akaike, "A New Look at the Statistical Model Identification," *IEEE Transactions on Automatic Control*, vol. 19, no. 6, pp. 716–723, 1974.

[46] K. P. Burnham and D. R. Anderson, *Model Selection and Multimodel Inference: A Practical Information-Theoretic Approach*. Springer New York, 2003.

[47] R. He, Z. Zhong, B. Ai, J. Ding, Y. Yang, and A. F. Molisch, "Short-term fading behavior in high-speed railway cutting scenario: Measurements, analysis, and statistical models," *IEEE Transactions on Antennas and Propagation*, vol. 61, no. 4, pp. 2209–2222, 2013.

[48] D. B. Williams, "Counting the Degrees of Freedom When Using AIC and MDL to Detect Signals," *IEEE Transactions on Signal Processing*, vol. 42, no. 11, pp. 3282–3284, 1994.

[49] S. Boyd and L. Vandenberghe, *Convex Optimization*. Cambridge University Press, 2004.

[50] D. H. Johnson and D. E. Dudgeon, *Array signal processing: concepts and techniques*. Simon & Schuster, 1992.

[51] A-INFO, "Data sheet for biconical antenna SZ-2003000/P," Tech. Rep. [Online]. Available: http://www.ainfoinc.com/en/pro_pdf/new_products/antenna/Bi-Conical Antenna/tr_SZ-2003000-P.pdf

[52] S. Mota, M. O. Garcia, A. Rocha, and F. Pérez-Fontán, "Clustering of the multipath radio channel parameters," in *Proceedings of the 5th European Conference on Antennas and Propagation (EUCAP)*, 2011, pp. 3232–3236.

[53] S. Salous, K. Haneda, H. Bogucka, J. Sykora, S. R. Boqué, H. Ahmadi, W. Kotterman, M. Rumney, E. Ström, C. Buratti, C. Anton-Haro, K. Witrisal, F. Kaltenberger, M. Beach, N. Cardona, and C. Oestges, "COST Action CA15104 First Scientific Annual Report," Tech. Rep., 2017.

[54] B. H. Fleury, P. Jourdan, and A. Stucki, "High-resolution channel parameter estimation for MIMO applications using the SAGE algorithm," in *2002 International Zurich Seminar on Broadband Communications Access - Transmission - Networking (Cat. No.02TH8599)*, 2002, pp. 30.1–30.9.

[55] G. Del Galdo, V. Algeier, N. Czink, and M. Haardt, "Spatial Localization of Scattering Objects from High-Resolution Parameter Estimates," in *NEWCOM-ACORN Workshop*, no. 1, 2006, pp. 1–21.

[56] J. Poutanen, K. Haneda, J. Salmi, V.-m. Kolmonen, A. Richter, P. Almers, and P. Vainikainen, "Development of measurement-based ray tracer for multi-link double directional propagation parameters," in *2009 3rd European Conference on Antennas and Propagation*, 2009, pp. 2622–2626.

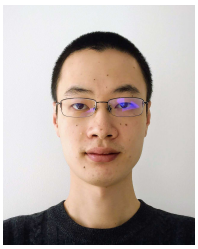

Yilin Ji received his B.Sc. degree in Electronics Science and Technology and M.Eng degree in Integrated Circuit Engineering from Tongji University, China, in 2013 and 2016, respectively. He is currently a Ph.D. fellow at the Antennas, Propagation and Millimeter-wave Systems (APMS) section at Aalborg University, Denmark. His main research areas are propagation channel characterization, indoor localization, and MIMO over-the-air testing.

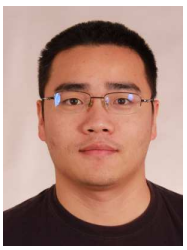

Wei Fan received his Bachelor of Engineering degree from Harbin Institute of technology, China in 2009, Masters double degree with highest honours from Politecnico di Torino, Italy and Grenoble Institute of Technology, France in 2011, and Ph.D. degree from Aalborg University, Denmark in 2014. From February 2011 to August 2011, he was with Intel Mobile Communications, Denmark as a research intern. He conducted a three-month internship at Anite telecoms oy, Finland in 2014. His main areas of research are over the air testing of multiple antenna systems, radio channel sounding, modelling and emulation. He is currently an associate professor at the Antennas, Propagation and Millimeterwave Systems (APMS) Section at Aalborg University.

Gert Frølund Pedersen was born in 1965 and married to Henriette and have 7 children. He received the B.Sc. E.E. degree, with honour, in electrical engineering from College of Technology in Dublin, Ireland in 1991, and the M.Sc. E.E. degree and Ph.D. from Aalborg University in 1993 and 2003. He has been with Aalborg University since 1993 where he is a full Professor heading the Antenna, Propagation and Networking LAB with 36 researcher. Further he is also the head of the doctoral school on wireless communication with some 100 phd students enrolled. His research has focused on radio communication for mobile terminals especially small Antennas, Diversity systems, Propagation and Biological effects and he has published more than 175 peer reviewed papers and holds 28 patents. He has also worked as consultant for developments of more than 100 antennas for mobile terminals including the first internal antenna for mobile phones in 1994 with lowest SAR, first internal triple-band antenna in 1998 with low SAR and high TRP and TIS, and lately various multi-antenna systems rated as the most efficient on the market. He has worked most of the time with joint university and industry projects and have received more than 12 M$ in direct research funding. Latest he is the project leader of the SAFE project with a total budget of 8 M$ investigating tunable front end including tunable antennas for the future multiband mobile phones. He has been one of the pioneers in establishing Over-The-Air (OTA) measurement systems. The measurement technique is now well established for mobile terminals with single antennas and he was chairing the various COST groups (swg2.2 of COST 259, 273, 2100 and now ICT1004) with liaison to 3GPP for over-the-air test of MIMO terminals. Presently he is deeply involved in MIMO OTA measurement.